

An Inertial Model of the General Circulation in an Ocean with Bottom Topography

Janet M. Becker

Department of Ocean Engineering, University of Hawaii, Honolulu, Hawaii

Abstract. The barotropic, wind-driven circulation in a basin bounded at the south by the equator and for which the ocean depth varies smoothly between a constant deep ocean value and zero at the coasts is examined numerically to analyze how inertia and topography affect theoretical models of the general circulation. As is well known, the inclusion of topography aligns the boundary currents along f/H contours. Increasing the wind forcing leads to unsteady inertial circulations that consist of periodic, modulated, and irregular eddy generation.

1. Introduction

The effects of topography on the general ocean circulation have long been recognized as important. The majority of theoretical ocean general circulation models, however, have been confined to flat bottom oceans or have invoked the quasi-geostrophic approximation. One assumption central to the quasi-geostrophic approximation is that variations in the fluid depth are small. As a result, the ocean depth typically is discontinuous at coastlines in these models. While many useful insights about ocean boundary currents have been gained from these theoretical models, open questions remain about how the boundary currents affect the gyre-scale circulation and about model sensitivity to frictional parameterizations (c.f. *Killworth* [1993], *Böning* [1986], *Cummins* [1992]). It may be that the sensitivity of these model circulations is in part due to the singular nature of the topography. We also remark that these models may not readily be extended to incorporate the important effects of finite amplitude topography.

A few theoretical studies have shown that the boundary currents obtained in an ocean with finite amplitude topography differ significantly from those obtained in an ocean with infinitesimal topographic variations (e.g. *Salmon* [1992]). These studies, however, largely have neglected the effects of inertia. In this note, we consider how inertia affects the barotropic circulation in an ocean for which the depth undergoes $O(1)$ variations to vanish smoothly at the coastlines. In section 2, we present the dynamics and review the steady linear circulations and in section 3, we determine how inertia modifies the linear circulation using numerical simulations.

2. Shallow water equations

We consider here the barotropic ocean circulation governed by (in nondimensional form)

$$\text{Ro} \frac{D\mathbf{u}}{Dt} + \mathbf{f} \times \mathbf{u} = -\nabla\phi - \varepsilon\mathbf{u} + \frac{\partial\tau}{\partial z} \quad (1)$$

$$\nabla \cdot \mathbf{u} + w_z = 0 \quad (2)$$

and subject to

$$w = 0(z = 0), w = -\mathbf{u} \cdot \nabla H(z = -H(x, y)), \quad (3)$$

and the condition that the normal component of the transport vanishes on the coastal boundaries. In (1-3), $(uvw) \equiv \mathbf{u}, w$ is the velocity in the (eastward, northward, vertical) direction with coordinates (x, y, z) ; $\mathbf{f} = y\mathbf{k}$ where y is the Coriolis parameter and \mathbf{k} the vertical unit vector; $\phi = p + gz$ where p is the pressure; $\tau = (\tau^x, \tau^y, 0)$ is the stress; $\text{Ro} = U / f_0 L$ is the Rossby number and $\varepsilon = \varepsilon_{Ra} / f_0$ is the dimensionless coefficient of Rayleigh friction. Here, we choose to balance the vorticity input by the wind with Rayleigh friction.

The nondimensional variables in (1-3) are scaled conventionally with horizontal/vertical length scales of $O(4000 \text{ km}/4 \text{ km})$, a representative flow speed U of $O(0.2 \text{ km/day})$ and $f_0 = \beta L = 10^{-4} \text{ sec}^{-1}$. We next define the transport stream function

$$(-\psi_y, \psi_x) = H(u, v) \quad (4)$$

which follows from (2-3) and combine the depth integrated versions of the horizontal components of (1) to form the vorticity equation

$$\text{Ro} \frac{\partial \zeta}{\partial t} + J \left(\psi, \frac{\text{Ro} \zeta + y}{H} \right) = -\varepsilon \zeta + W \quad (5)$$

which is subject to $\psi = 0$ on the coastal boundaries. In (5), $\zeta \equiv v_x - u_y = \nabla_h \cdot (H^{-1} \nabla_h \psi)$ is the relative vorticity (∇_h is the horizontal gradient operator), $W \equiv \nabla \times$

For a flat bottom ocean with $H(x,y) = 1$, the steady, linear circulation of (5) is described in the classic work of Stommel [1948] and consists of an interior wind driven (Sverdrup) flow that is closed by a frictional western boundary current of width ϵ . For an ocean in which the depth goes to zero smoothly at the coast, the western boundary current system is asymptotically independent of the friction and the flow on the continental slope is determined by y/H and by the interior flow (e.g., Salmon [1992, 1994]). We also remark that the circulation in a basin bounded at the south by the equator (for which y/H lines converge at the equatorial point on the western boundary) differs significantly from that in a basin with a southern coastal boundary (for which closed contours of y/H exist) (c.f. Kawase [1993]). Here, only the more realistic equatorial case is considered.

The steady, linear ($Ro = 0$) circulation described by (5) is presented in Figure 1 for a flat bottom ocean and in Figure 2 for an ocean with western and northern continental shelves. The topography, $H(x,y)$, used in all of the experiments (except Figure 1) is presented in Figure 3 (left). In this initial study, the wind stress curl simply is taken as

$$W(x,y) = \begin{cases} -\sin\left(\frac{4\pi}{3}\left(y - \frac{1}{2}\right)\right) & 1/2 < y \leq 2 \\ 0 & 0 \leq y \leq 1/2 \end{cases} \quad (6)$$

in all experiments. The coefficient of Rayleigh friction corresponds to a Stommel layer of one grid point. In the absence of topography, the circulation consists of two symmetric, counter-rotating gyres (Figure 1, left) and the vorticity field (Figure 1, right) consists of two isolated, oppositely signed layers concentrated at the western boundary. In contrast, the linear circulation in the basin

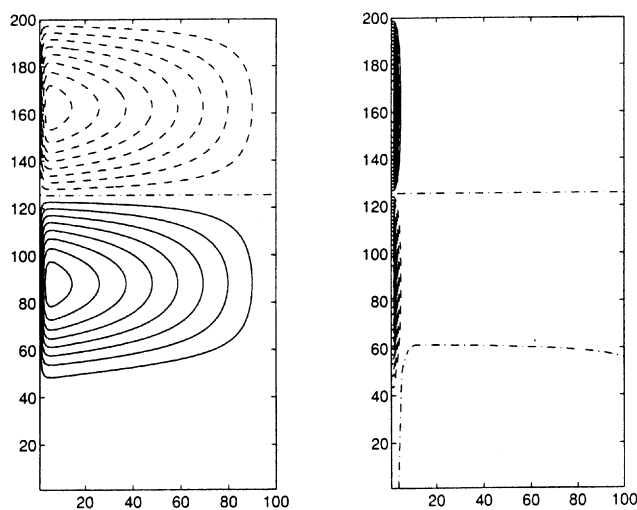


Figure 1. (left) The transport stream function ψ and (right) vorticity ζ that satisfy (5) for $Ro = 0$, $\epsilon = 0.01$, $H(x,y) = 1$ and the wind stress curl given by (6). In all figures, the solid/dashed/dot-dash contours correspond to positive/negative/zero values and the contour interval for $\psi/H\zeta$ is $0.1/100$.

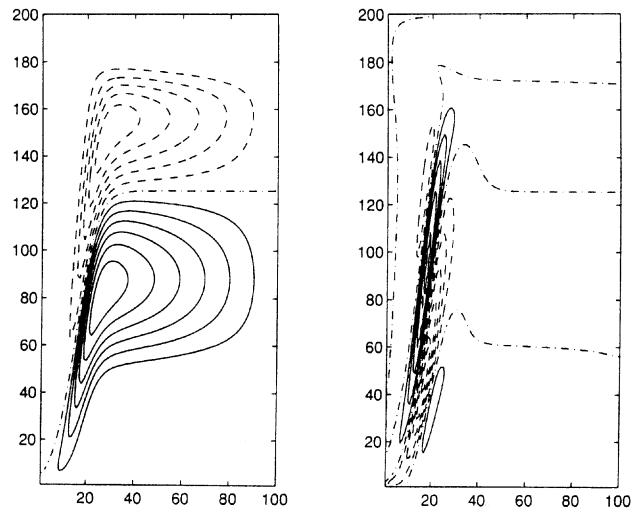


Figure 2. (left) The transport stream function ψ and (right) vorticity (multiplied by the ocean depth, see footnote 1) $H\zeta$ for the conditions of Figure 1, but with the $H(x,y)$ of Figure 3.

with topography is asymmetric and may be understood by viewing (5) as an advection-diffusion equation for ψ with advecting velocity $\mathbf{k} \times \nabla(y/H)$ and $-W$ the source (c.f. Salmon [1992]). The “streamlines” of this “flow” are presented in Figure 3, right. The difference between the linear topographic and flat bottom circulation is clearly exhibited in the vorticity¹ field. In the flat bottom ocean, the vortex layers are symmetric and isolated, while in the ocean with topography, the layers are asymmetric and aligned along y/H contours.

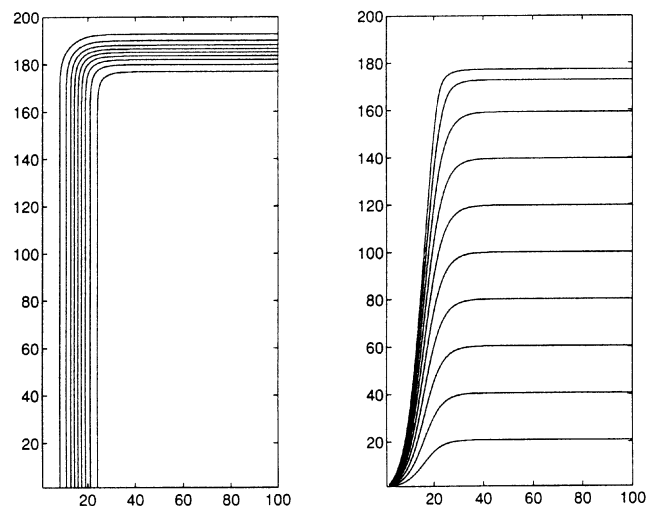


Figure 3. (left) The ocean depth $H(x,y)$ which varies smoothly from zero at the western and northern coasts to unity in the interior. (right) The corresponding contours of y/H .

¹ Due to large values of the vorticity in the southwest corner of the basin, contours of $H\zeta$ are presented here.

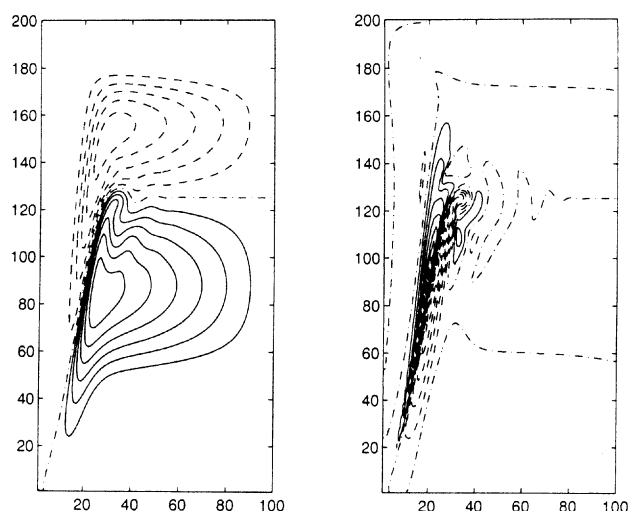


Figure 4. Steady, inertial circulation. (left) ψ and (right) $H\zeta$ for the conditions of Figure 2 but with $Ro = 0.0002$.

3. Numerical Model

To determine how inertia affects the linear, topographic circulation described above, we solve (5) numerically using a finite-difference method. We time-step (5) to analyze unsteady dynamical processes and to determine the stability of the steady circulations.

Inertial numerical models of the general ocean circulation require a subgrid-scale closure scheme to parameterize the effects of the scales of motion not resolved by the numerical grid. Here, we use an implicit closure scheme to finite difference the advective terms in

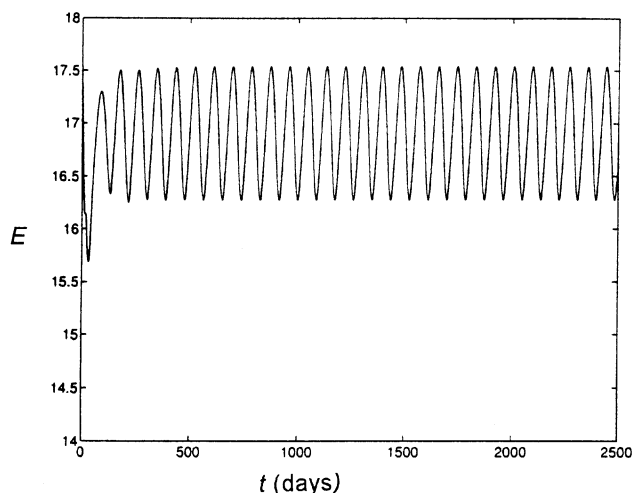


Figure 5. Time-series of the basin integrated total energy E , (7) for the conditions of Figure 2 but with $Ro = 0.0005$. The period of eddy formation is $O(100)$ days.

(5) for which the truncation error corresponds to a biharmonic operator on ζ in the interior, but requires no additional boundary conditions (third-order upwind differencing, Leonard [1984]).

The numerical solutions of (5) are presented for a rectangular ocean basin contained in $0 \leq x \leq 1$, $0 \leq y \leq 2$. As discussed above, the southern boundary of this model ocean is the equator where the boundary conditions of cross-equatorial symmetry of the dynamics, forcing and topography are applied. The form of the wind stress curl, (6), is chosen for simplicity and to reduce the computing time necessary to obtain steady-state, nonlinear solutions. For all runs shown, the resolution is 100×200 and $\epsilon = 0.01$ (but see below).

The effects of weak nonlinearity may be understood by considering how advection affects the steady, linear circulation presented in Figures 1 and 2. For the flat bottom ocean, the effects of weak nonlinearity are well known, and, for example, for the subtropical gyre, negative relative vorticity is advected from the south to the north. Then, to dissipate their excess negative relative vorticity, fluid parcels overshoot the latitude where they rejoin the Sverdrup interior. For a two gyre circulation in a flat bottom ocean, inertia results in the isolated, symmetric vortex layers being pulled off the western boundary and aligned along the latitude of zero wind stress curl where vortex interactions then may occur. For an ocean with finite amplitude topography, however, we emphasize that the asymmetric vortex layers are aligned in the linear approximation. Then, the introduction of inertia causes the vortex layers to advect each other northeastward (along the axis of alignment), and additionally, to draw the weaker layer around the stronger layer. This behavior is exhibited by the steady inertial solution presented in Figure 4 for which $Ro = 0.0002$. Advection of vorticity has reduced the southwestward extent of the tails of the gyres and the asymmetry in the strength of the vortex layers has resulted in the bending observed at the northern limit of these layers.

By increasing the magnitude of the wind ($Ro = 0.0005$), the advection becomes strong enough to wrap around and pinch off an eddy from the weaker (positive) vorticity layer. This eddy formation occurs periodically as may be seen in a time-series of a finite difference approximation of the basin integrated total energy

$$E = \iint \frac{1}{2H} \nabla \psi \cdot \nabla \psi dA \quad (7)$$

for $Ro = 0.0005$ (Figure 5). We note that the period of the eddy formation is $O(100)$ days. Figure 6 presents snapshots of this process at quarter period intervals. The pinching off of an eddy occurs near an energy maxima.

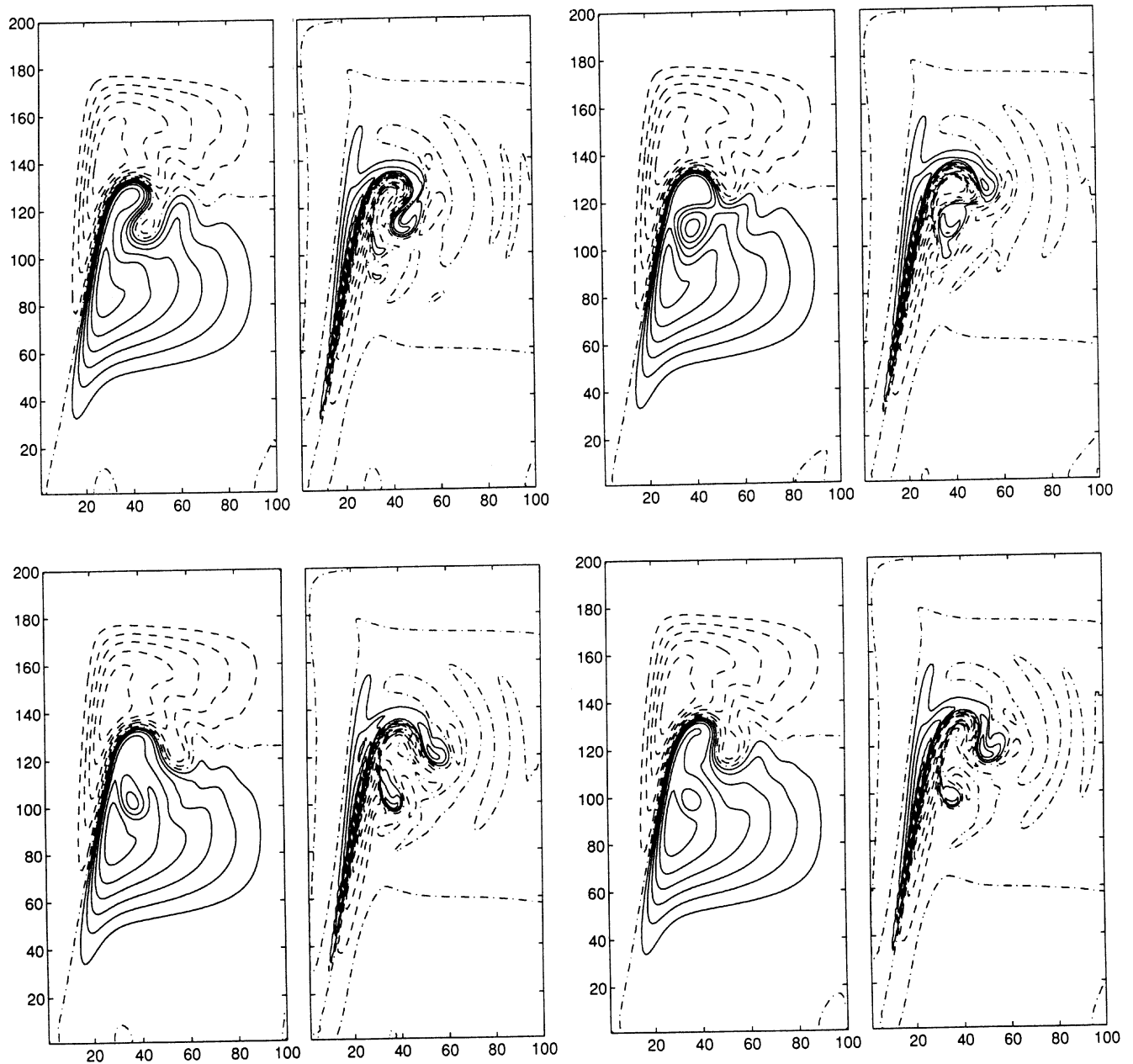


Figure 6. The periodic pinching off of an eddy for the conditions of Figure 5. Snapshots of ψ (left) and $H\zeta$ (right) at times corresponding to (top left) maximum energy, (top right) approximately one quarter period past the maximum, (bottom left) minimum energy, and (bottom right) approximately one quarter period past the minimum.

A further increase in the wind ($Ro = 0.001$) results in aperiodic eddy formation.² Here, in addition to an eddy of positive vorticity being entrained in the subtropical gyre, an eddy of negative vorticity is entrained subsequently in the subpolar gyre. A time-series of E for $Ro = 0.001$ (Figure 7) consists of a high frequency carrier signal modulated by a lower frequency envelope. The

minima in the low frequency envelope appears to correspond to the two eddies pinching off nearly simultaneously. Snapshots of the circulation exhibiting the formation of the positive and negative vorticity eddies are presented in Figure 8. Increasing the wind further results in more complicated unsteady behavior (not shown).

²We emphasize that a spectral analysis of this process has not yet been conducted and will be presented in a future work.

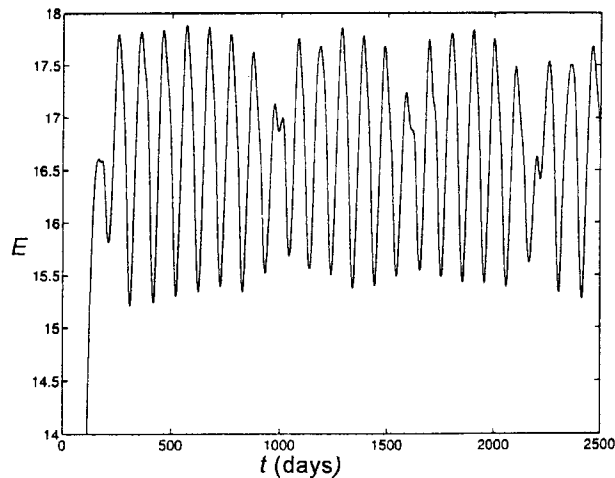


Figure 7. The time-series of E , (7) for the conditions of Figure 2 but with $Ro = 0.001$.

We remark that the qualitative character of the results presented above appear to be independent of the model resolution in the sense that for coarser or finer resolutions, the sequence of steady circulation, periodic, modulated and irregular unsteady eddy formation still occur, but for different Rossby numbers (i.e., for $Ro = 0.001$ and 50×100 resolution, the eddy formation is periodic while for 200×400 resolution, the eddy formation is irregular). A future study will report model sensitivity studies in more detail.

Acknowledgments. I am indebted to Rick Salmon for helpful discussions and for the final numerical model. This work was supported in part by an NSF Mathematical Sciences Postdoctoral Research Fellowship and a URC seed money award from the University of Hawaii. School of Ocean and Earth Science and Technology contribution no. 3915.

References

- Böning, C.W., 1986: On the influence of frictional parameterization in wind-driven ocean circulation models, *Dyn. Atmos. Oceans*, 10, 63-92.
- Cummins, P.F., 1992: Inertial gyres in decaying and forced geostrophic turbulence, *J. Mar. Res.*, 50, 545-566.
- Kawase, M., 1993: Effects of a Concave Bottom Geometry on the Upwelling-driven Circulation in an Abyssal Ocean Basin, *J. Phys. Oceanogr.*, 23, 400-405.
- Killworth, P.D., 1993: On the Role of Dissipation in Inertial Western Boundary Currents, *J. Phys. Oceanogr.*, 23, 539-553.
- Leonard, B.P., 1984: Third-order upwinding as a rational basis for computational fluid dynamics, in *Computational Techniques and Applications: CTAC-83*, J. Noye and C. Fletcher, eds. Elsevier North-Holland, 106-120.
- Salmon, R., 1992: A two-layer Gulf Stream over a continental slope, *J. Mar. Res.*, 50, 341-365.
- Salmon, R., 1994: Generalized two-layer models of ocean circulation, *J. Mar. Res.*, 52, 865-908.
- Stommel, H., 1948: The westward intensification of wind-driven ocean currents, *Trans. Am. Geophys. Union*, 29, 202-206.

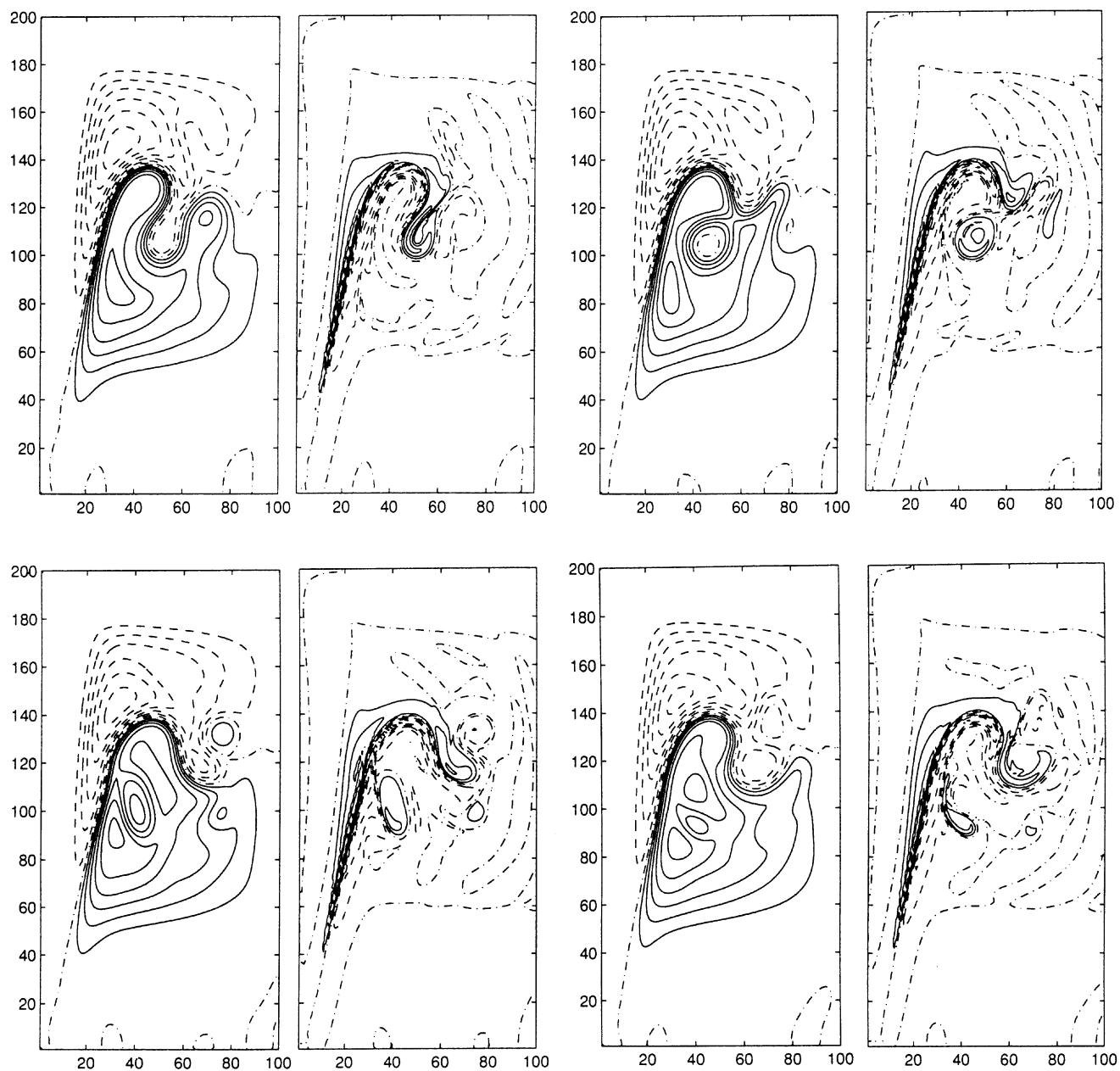


Figure 8. Snapshots of ψ and $H\zeta$ for the conditions of Figure 7 at these times: (upper left) 1184 days (approximately a local maxima of the energy), (upper right) 1201 days, (lower left) 1220 days, and (lower right) 1238 days (approximately a local minima of the energy).